TABLE 1

Protein expression levels of metabolizing enzymes in microsomal fraction of humanized liver of PXB mice

Unit of protein expression is pmol/mg protein of microsomal fraction.

Donor	ALL (n =11)				BD85 (n = 5)				BD72 (n = 3)				BD87 (n = 3)			
	Mean	S.D.	%CV	n	Mean	S.D.	% CV	n	Mean	S.D.	%CV	n	Mean	S.D.	%CV	n
CYP2E1	51.8	9.7	18.7	11	51.7	9.4	18	5	52.9	7.8	15	3	50.9	15.2	30	3
CYP3A4	27.8	12.4	44.5	11	26.7	11.1	41	5	24.8	10.7	43	3	32.4	18.9	58	3
CYP2C9*	21.7	14.2	65.5	11	9.71	1.00	10	5	28.6	10.6	37	3	34.8	14.4	41	3
CYP1A2	20.7	6.4	30.9	11	23.3	5.1	22	5	16.5	7.1	43	3	20.4	7.7	38	3
CYP2C8*	15.8	6.3	39.8	11	10.2	1.8	18	5	16.9	1.9	11	3	24.1	2.1	9	3
CYP2A6*	10.2	7.8	76.1	11	2.93	0.40	14	5	12.4	1.6	13	3	20.2	3.3	16	3
CYP2C19*	8.84	6.25	70.8	11	4.90	1.15	24	5	16.6	7.2	43	3	7.59	2.99	39	3
CYP2D6*	7.07	2.94	41.6	9	6.77	1.64	24	5	1.23			1	9.51	1.75	18	3
CYP3A7	6.32	3.31	52.3	5	6.32	3.31	52	5	LLOQ				LLOQ			
CYP3A5	5.56	4.09	73.5	6	6.56	3.66	56	5	LLOQ				0.579			1
CYP4A11	5.04	1.97	39.1	9	4.85	1.99	41	5	2.29			1	6.26	1.24	20	3
CYP2B6*	1.90	0.91	47.6	11	1.68	0.49	30	5	1.08	0.27	25	3	3.11	0.45	15	3
P450R*	31.6	18.7	59.3	11	12.4	1.7	14	5	43.7	4.6	11	3	51.2	1.7	3	3
UGT2B7	55.0	20.8	37.8	6	N.D.				43.0	11.4	26	3	67.0	22.7	34	3
UGT1A1	19.0	2.4	12.5	6	N.D.				19.7	3.5	18	3	18.4	0.5	3	3
Na$^+$/K$^+$ ATPase	10.4	1.5	14.5	11	9.94	2.14	22	5	10.5	0.4	4	3	11.1	0.9	8	3
γ-GTP	2.64	0.37	14.1	11	2.57	0.33	13	5	2.64	0.55	21	3	2.74	0.37	13	3

n, Number of determined samples; LLOQ, lower than the limit of quantification; N.D., not determined.
*Significant difference ($P < 0.05$) in protein expression levels among donors (BD85, BD72, and BD87).

donors. This suggests that the purity of plasma membrane fraction was similar among donors, although the variability appeared to be greater than that of the microsomal fraction

All human transporters, except breast cancer resistance protein (BCRP), were quantified in all 11 samples (Table 2). MDR3 and BSEP exhibited the highest expression levels among the quantified transporters at 8.68 and 7.57 pmol/mg plasma membrane protein, respectively. Human BCRP was not detected in five samples from donor BD85, and was not quantified in samples from BD72 and BD87, in accordance with a report that BCRP expression is very low in human liver plasma membrane fraction (Ohtsuki et al., 2012). The average value of %CV of all samples was 47.0%, which was similar to

that of microsomal fraction (43.4%), and significantly greater than that of BD72 (25.5%, $P < 0.01$) or BD87 (25.6%, $P < 0.01$). It was also greater, though not significantly, than that of BD85 (35.4%). Therefore, differences among the donors appear to contribute substantially to the variances of protein expression levels in all samples. MDR3, BSEP, MRP2, ABCG8, OCT1, and OATP1B3 showed significantly different protein expression levels depending on the hepatocyte donors ($P < 0.05$).

Comparison of Protein Expression Levels in Liver of PXB Mice and Human. The protein expression levels of metabolizing enzymes and transporters in PXB mouse liver shown in Tables 1 and 2 were compared with those in human liver. The protein expression levels

TABLE 2

Protein expression levels of transporters in plasma membrane fraction of humanized liver of PXB mice

Unit of protein expression is pmol/mg protein of plasma membrane fraction.

Donor	ALL (n = 11)				BD85 (n = 5)				BD72 (n = 3)				BD87 (n = 3)			
	Mean	S.D.	%CV	n	Mean	S.D.	%CV	n	Mean	S.D.	%CV	n	Mean	S.D.	%CV	n
Canalicular localized transporter																
MDR3/ABCB4*	8.68	7.32	84.3	11	4.19	1.29	31	5	7.47	3.66	49	3	17.4	9.24	53	3
BSEP/ABCB11*	7.57	7.91	104	11	3.06	1.13	37	5	6.12	2.79	46	3	16.5	11.29	68	3
MDR1/ABCB1	4.71	1.78	37.7	11	4.30	1.55	36	5	3.86	1.19	31	3	6.26	2.10	34	3
MRP2/ABCC2*	2.37	0.88	37.1	11	2.06	0.91	44	5	1.89	0.19	10	3	3.36	0.34	10	3
MATE1	1.10	0.22	19.7	11	1.07	0.23	22	5	1.28	0.21	17	3	0.981	0.086	9	3
ABCG8*	0.956	0.701	73.3	11	0.417	0.106	25	5	1.89	0.62	33	3	0.921	0.132	14	3
BCRP/ABCG2	LLOQ				LLOQ				N.D.				N.D.			
γ-GTP	2.22	0.89	40.1	11	2.52	0.60	24	5	1.57	0.18	12	3	2.39	1.52	64	3
Sinusoidal localized transporter																
OCT1*	4.21	3.41	81.0	11	6.87	3.04	44	5	3.22	1.61	50	3	0.765	0.102	13	3
OAT2	4.09	1.18	28.8	11	4.89	1.08	22	5	3.76	1.06	28	3	3.09	0.49	16	3
NTCP	2.42	0.81	33.5	11	2.12	1.12	53	5	2.61	0.34	13	3	2.71	0.47	17	3
MRP6	2.29	0.51	22.2	11	2.57	0.58	23	5	1.97	0.48	25	3	2.14	0.08	4	3
OATP1B1	1.45	0.56	38.9	11	1.22	0.63	52	5	1.50	0.16	11	3	1.78	0.68	38	3
OATP1B3*	1.03	0.47	45.9	11	0.616	0.207	34	5	1.47	0.47	32	3	1.28	0.06	5	3
OATP2B1	0.578	0.241	42.5	11	0.684	0.320	47	5	0.500	0.119	24	3	0.442	0.090	20	3
Na$^+$/K$^+$ ATPase	22.6	6.65	29.4	11	23.6	9.00	38	5	22.0	1.7	8	3	21.7	7.22	33	3
Localization unknown																
ENT1	1.55	0.50	32.6	11	1.79	0.60	34	5	1.59	0.32	20	3	1.11	0.13	11	3

n, Number of determined samples; LLOQ, lower than the limit of quantification; N.D., not determined; ENT, equilibrative nucleoside transporter; NTCP, sodium/taurocholate cotransporting polypeptide.
*Significant difference ($P < 0.05$) in protein expression levels among donors (BD85, BD72 and BD87).

determined in 17 human liver biopsies (eight males and nine females, ages 20–74) were taken from our previous report (Ohtsuki et al., 2012). In the human liver biopsies, metabolizing enzymes and transporters were quantified in both microsomal fraction and plasma membrane fraction, as in the case of PXB mice. Expression levels of molecules determined both in PXB mouse and human livers are compared in Fig. 1. The differences between PXB mouse liver and human liver for all compared metabolizing enzymes and transporters were within 4-fold, except for CYP2A6 and CYP4A11 among metabolizing enzymes, and MDR3 and BSEP among transporters. Protein expression levels of CYP2A6 and CYP4A11 in PXB mouse liver microsomal fraction were 5.50- and 4.33-fold lower than those in human liver microsomal fraction, respectively. In contrast, protein expression levels of BSEP and MDR3 in PXB mouse liver plasma membrane fraction were 5.12- and 4.62-fold greater than those in human liver plasma membrane fraction.

Discussion

In the present study, we investigated the protein expression levels of human metabolizing enzymes in microsomal fraction and human membrane transporters in plasma membrane of humanized liver of PXB mice using LC-MS/MS–based protein quantification. In total, 11 livers of PXB mice humanized with hepatocytes from three different donors were quantified. Our results indicate that differences in the human donors contributed substantially to the variations of measured protein expression levels (Tables 1 and 2). This seems reasonable because the PXB mice were bred under controlled conditions, whereas the human donors might have been exposed to a variety of different environmental factors, such as food and drug intake, that could affect the expression of metabolizing enzymes and transporters.

Protein expression of CYP3A5 and CYP3A7 was detected in all liver samples from only one donor (BD85), and protein expression of CYP2D6 was detected in all liver samples from two donors (BD72 and BD87) (Table 1). In the previous study with PXB mice from two donors, CYP3A5 protein expression levels were very low in liver from both donors, and the reason for its low expression was genetic polymorphisms of the donor hepatocytes (Katoh et al., 2004). In our previous report, liver biopsies were clearly classified into two groups: a high-CYP3A7 group and a very low CYP3A7 group (Ohtsuki et al., 2012). Hence, the large differences in protein expression levels of these molecules might be attributable to differences in the genetic background of donor hepatocytes, although it is not known whether single-nucleotide polymorphisms were present in the transplanted human hepatocytes in our study. These results suggest that it is important to characterize the donor hepatocytes in studies with PXB mice; in principle, experiments should be performed with PXB mice humanized with hepatocytes from the same donor to ensure comparability of data.

In our previous reports, individual differences of BSEP protein expression were not large in plasma membrane fraction of human liver; the %CV was 29.7% among 17 liver biopsies (Ohtsuki et al., 2012). In contrast, %CV of BSEP protein expression was 105% in PXB liver (Table 2). A possible explanation is that BSEP expression is highly regulated in human liver, but lack of human-specific regulation in PXB mice resulted in a very high variance of protein expression. Interestingly, differences in MDR3 protein levels according to donor showed a trend similar to those of BSEP (Table 2). BSEP and MDR3 are cooperatively involved in excretion of lipids, and are regulated by FXR (Oude Elferink and Paulusma, 2007). Interspecies differences in FXR response have been reported (Cui et al., 2002; Song et al., 2013). Although further studies are necessary, it was possible that a shared

regulatory mechanism of BSEP and MDR3 played some role in the interdonor differences.

The present study demonstrated that protein expression levels of most of the quantified metabolizing enzymes and transporters were within a 4-fold range from those in the same fraction of human liver reported previously (Ohtsuki et al., 2012) (Fig. 1). This range of
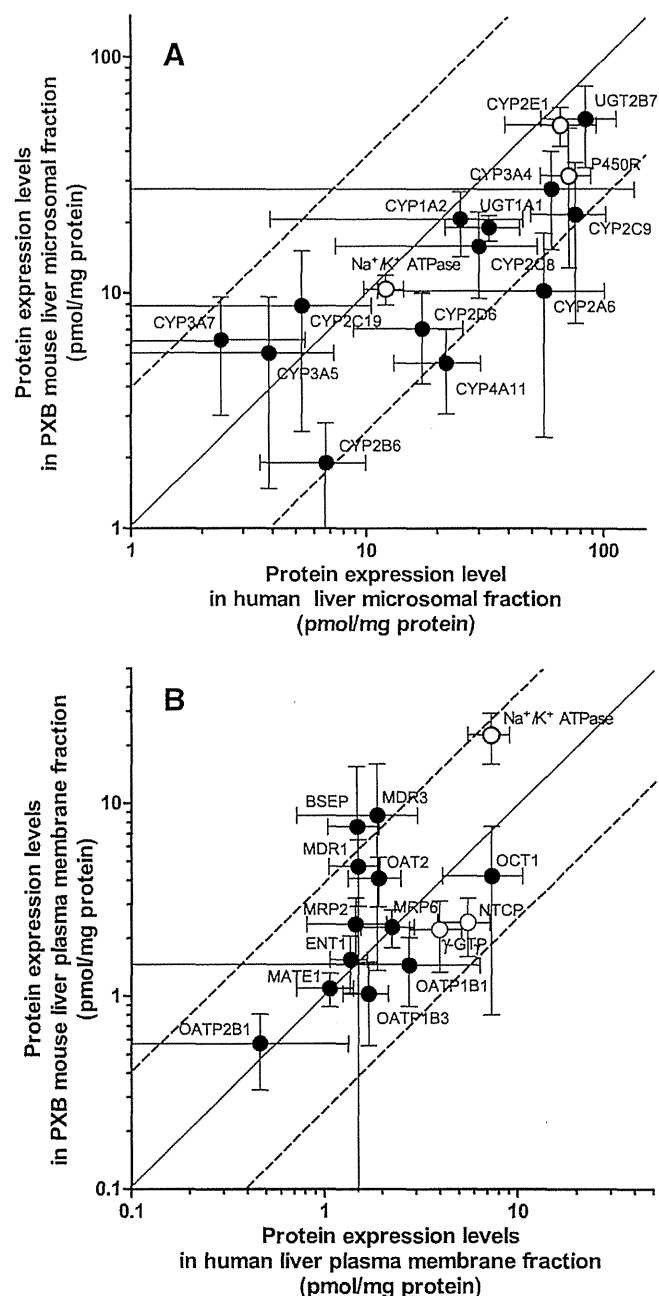

Fig. 1. Comparison of protein expression levels of metabolizing enzymes in microsomal fraction and transporters in plasma membrane fraction between humanized liver of PXB mice and human liver. Protein expression levels of metabolizing enzymes and transporters were determined in microsomal fraction (A) and plasma membrane fraction (B), respectively, of humanized liver of PXB mice, as shown in Tables 1 and 2 (mean ± S.D.). The data for microsomal fraction of 17 human liver biopsies (mean ± S.D.) were taken from our previous report (Ohtsuki et al., 2012). The solid line passing through the origin represents the line of identity, and the broken lines represent 4-fold differences. Open symbols indicate quantification values obtained with peptides that are conserved in the human and mouse proteins.

difference was the same as that in average expression levels among the three donors. The enzyme activities of P450 enzymes were reported to be better correlated to protein expression levels in the microsomal fraction than to mRNA expression levels (Ohtsuki et al., 2012). We compared the protein expression levels of transporters between PXB mice and human in plasma membrane fraction, where the quantified transporters function. A large species difference was reported in protein expression levels of BCRP in plasma membrane fraction: 0.419 pmol/mg protein in human liver and 8.51 pmol/mg protein in mouse liver (Kamiie et al., 2008; Ohtsuki et al., 2012). Here, human BCRP was under the limit of quantification in humanized liver of PXB mice, indicating that human hepatocytes retain the characteristic low expression of BCRP in PXB mice. Overall, our results indicate that humanized liver in PXB mice well retains the protein expression pattern of metabolizing enzymes and transporters of human liver.

Our previous report demonstrated that, in sandwich-cultured human hepatocytes, differences of protein expression levels of metabolizing enzymes and transporters compared with those in human liver were within a 5-fold range (Schaefer et al., 2012). A similar range of difference was found in liver of PXB mice in this study, though in cultured human hepatocytes, the protein expression levels of transporters tended to be greater than those in human liver. Since humanized liver retains the structure of human liver tissue (Tateno et al., 2013), our results suggest that humanized liver of PXB mice is a useful model for analyzing human hepatic drug metabolism in vivo.

In conclusion, we measured the protein expression levels of metabolizing enzymes in microsomal fraction and transporters in plasma membrane fraction of humanized liver of chimeric PXB mice. The protein expression levels of the quantified metabolizing enzymes and transporters well reflected those of the donor human liver. The protein expression in humanized liver was significantly affected by the background of each individual donor. Our results indicate that humanized liver of PXB mice is a useful model of human liver, but it is important to note that interpretation of the results obtained from PXB mice requires a knowledge of not only the value of the replacement index, but also information about the background of the hepatocyte donor.

Department of Pharmaceutical Microbiology, Faculty of Life Sciences, Kumamoto University, Kumamoto, Japan (S.O., K.N.); Laboratory of Veterinary Pathology, School of Veterinary Medicine, Azabu University, Kanagawa, Japan (H.K., J.K.); Division of Membrane Transport and Drug Targeting, Graduate School of Pharmaceutical Sciences, Tohoku University, Sendai, Japan (T.I, Y.K., W.O., Y.U., T.T.); PhoenixBio, Co., Ltd., Hiroshima, Japan (C.T.); DeThree Research Laboratory Inc., Ibaraki, Japan (T.H.)

SUMIO OHTSUKI
HIROTAKA KAWAKAMI
TAE INOUE
KENJI NAKAMURA
CHISE TATENO
YUKI KATSUKURA
WATARU OBUCHI
YASUO UCHIDA
JUNICHI KAMIIE
TORU HORIE
TETSUYA TERASAKI

Authorship Contributions

Participated in research design: Ohtsuki, Tateno, Kamiie, Horie, Terasaki.
Conducted experiments: Kawakami, Inoue, Nakamura, Katsukura.
Contributed new reagents or analytic tools: Obuchi, Uchida.
Performed data analysis: Ohtsuki, Kawakami, Inoue, Nakamura.

Wrote or contributed to the writing of the manuscript: Ohtsuki, Tateno, Horie, Terasaki.

References

Cui J, Heard TS, Yu J, Lo JL, Huang L, Li Y, Schaeffer JM, and Wright SD (2002) The amino acid residues asparagine 354 and isoleucine 372 of human farnesoid X receptor confer the receptor with high sensitivity to chenodeoxycholate. *J Biol Chem* 277:25963–25969.

De Serres M, Bowers G, Boyle G, Beaumont C, Castellino S, Sigafoos J, Dave M, Roberts A, Shah V, and Olson K, et al. (2011) Evaluation of a chimeric (uPA+/+)/SCID mouse model with a humanized liver for prediction of human metabolism. *Xenobiotica* 41:464–475.

Hasegawa M, Tahara H, Inoue R, Kakuni M, Tateno C, and Ushiki J (2012) Investigation of drug-drug interactions caused by human pregnane X receptor-mediated induction of CYP3A4 and CYP2C subfamilies in chimeric mice with a humanized liver. *Drug Metab Dispos* 40:474–480.

Inoue T, Sugihara K, Ohshita H, Horie T, Kitamura S, and Ohta S (2009) Prediction of human disposition toward S-3H-warfarin using chimeric mice with humanized liver. *Drug Metab Pharmacokinet* 24:153–160.

Kamiie J, Ohtsuki S, Iwase R, Ohmine K, Katsukura Y, Yanai K, Sekine Y, Uchida Y, Ito S, and Terasaki T (2008) Quantitative atlas of membrane transporter proteins: development and application of a highly sensitive simultaneous LC/MS/MS method combined with novel in-silico peptide selection criteria. *Pharm Res* 25:1469–1483.

Kamimura H, Nakada N, Suzuki K, Mera A, Souda K, Murakami Y, Tanaka K, Iwatsubo T, Kawamura A, and Usui T (2010) Assessment of chimeric mice with humanized liver as a tool for predicting circulating human metabolites. *Drug Metab Pharmacokinet* 25:223–235.

Katoh M, Matsui T, Nakajima M, Tateno C, Kataoka M, Soeno Y, Horie T, Iwasaki K, Yoshizato K, and Yokoi T (2004) Expression of human cytochromes P450 in chimeric mice with humanized liver. *Drug Metab Dispos* 32:1402–1410.

Katoh M, Matsui T, Okumura H, Nakajima M, Nishimura M, Naito S, Tateno C, Yoshizato K, and Yokoi T (2005) Expression of human phase II enzymes in chimeric mice with humanized liver. *Drug Metab Dispos* 33:1333–1340.

Kawakami H, Ohtsuki S, Kamiie J, Suzuki T, Abe T, and Terasaki T (2011) Simultaneous absolute quantification of 11 cytochrome P450 isoforms in human liver microsomes by liquid chromatography tandem mass spectrometry with in silico target peptide selection. *J Pharm Sci* 100:341–352.

Kikuchi R, McCown M, Olson P, Tateno C, Morikawa Y, Katoh Y, Bourdet DL, Monshouwer M, and Fretland AJ (2010) Effect of hepatitis C virus infection on the mRNA expression of drug transporters and cytochrome p450 enzymes in chimeric mice with humanized liver. *Drug Metab Dispos* 38:1954–1961.

Nishimura M, Yoshitsugu H, Yokoi T, Tateno C, Kataoka M, Horie T, Yoshizato K, and Naito S (2005) Evaluation of mRNA expression of human drug-metabolizing enzymes and transporters in chimeric mouse with humanized liver. *Xenobiotica* 35:877–890.

Ohtsuki S, Uchida Y, Kubo Y, and Terasaki T (2011) Quantitative targeted absolute proteomics-based ADME research as a new path to drug discovery and development: methodology, advantages, strategy, and prospects. *J Pharm Sci* 100:3547–3559.

Ohtsuki S, Schaefer O, Kawakami H, Inoue T, Liehner S, Saito A, Ishiguro N, Kishimoto W, Ludwig-Schwellinger E, and Ebner T, et al. (2012) Simultaneous absolute protein quantification of transporters, cytochromes P450, and UDP-glucuronosyltransferases as a novel approach for the characterization of individual human liver: comparison with mRNA levels and activities. *Drug Metab Dispos* 40:83–92.

Oude Elferink RP and Paulusma CC (2007) Function and pathophysiological importance of ABCB4 (MDR3 P-glycoprotein). *Pflugers Arch* 453:601–610.

Schaefer O, Ohtsuki S, Kawakami H, Inoue T, Liehner S, Saito A, Sakamoto A, Ishiguro N, Matsumaru T, and Terasaki T, et al. (2012) Absolute quantification and differential expression of drug transporters, cytochrome P450 enzymes, and UDP-glucuronosyltransferases in cultured primary human hepatocytes. *Drug Metab Dispos* 40:93–103.

Shawahna R, Uchida Y, Declèves X, Ohtsuki S, Yousif S, Dauchy S, Jacob A, Chassoux F, Daumas-Duport C, and Couraud PO, et al. (2011) Transcriptomic and quantitative proteomic analysis of transporters and drug metabolizing enzymes in freshly isolated human brain microvessels. *Mol Pharm* 8:1332–1341.

Song X, Chen Y, Valanejad L, Kaimal R, Yan B, Stoner M, and Deng R (2013) Mechanistic insights into isoform-dependent and species-specific regulation of bile salt export pump by farnesoid X receptor. *J Lipid Res* 54:3030–3044.

Tateno C, Yoshizane Y, Saito N, Kataoka M, Utoh R, Yamasaki C, Tachibana A, Soeno Y, Asahina K, and Hino H, et al. (2004) Near completely humanized liver in mice shows human-type metabolic responses to drugs. *Am J Pathol* 165:901–912.

Tateno C, Miya F, Wake K, Kataoka M, Ishida Y, Yamasaki C, Yanagi A, Kakuni M, Wisse E, and Heyen F, et al. (2013) Morphological and microarray analyses of human hepatocytes from xenogeneic host livers. *Lab Invest* 93:54–71.

Uchida Y, Ohtsuki S, Katsukura Y, Ikeda C, Suzuki T, Kamiie J, and Terasaki T (2011) Quantitative targeted absolute proteomics of human blood-brain barrier transporters and receptors. *J Neurochem* 117:333–345.

Yamazaki H, Kuribayashi S, Inoue T, Tateno C, Nishikura Y, Oofusa K, Harada D, Naito S, Horie T, and Ohta S (2010) Approach for in vivo protein binding of 5-n-butyl-pyrazolo[1,5-a] pyrimidine bioactivated in chimeric mice with humanized liver by two-dimensional electrophoresis with accelerator mass spectrometry. *Chem Res Toxicol* 23:152–158.

Address correspondence to: Dr. Tetsuya Terasaki, Division of Membrane Transport and Drug Targeting Laboratory, Department of Biochemical Pharmacology and Therapeutics, Graduate School of Pharmaceutical Sciences, Tohoku University, 6-3 Aoba, Aramaki, Aoba-ku Sendai 980-8578, Japan. E-mail: terasaki.tetsuya@m.tohoku.ac.jp

Stem Cell Reports

ISSCR

Resource

—OPEN ACCESS

Precise Correction of the Dystrophin Gene in Duchenne Muscular Dystrophy Patient Induced Pluripotent Stem Cells by TALEN and CRISPR-Cas9

Hongmei Lisa Li,[1] Naoko Fujimoto,[1,2] Noriko Sasakawa,[1] Saya Shirai,[1] Tokiko Ohkame,[1] Tetsushi Sakuma,[4] Michihiro Tanaka,[1] Naoki Amano,[1] Akira Watanabe,[1] Hidetoshi Sakurai,[1] Takashi Yamamoto,[4] Shinya Yamanaka,[1,2,5] and Akitsu Hotta[1,2,3,*]

[1]Center for iPS Cell Research and Application, Kyoto University, Kyoto 606-8507, Japan
[2]iCeMS, Kyoto University, Kyoto 606-8501, Japan
[3]PRESTO, Japan Science and Technology Agency, Kawaguchi 332-0012, Japan
[4]Department of Mathematical and Life Sciences, Graduate School of Science, Hiroshima University, Higashi-Hiroshima 739-8526, Japan
[5]Gladstone Institute of Cardiovascular Disease, San Francisco, CA 94158, USA
*Correspondence: akitsu.hotta@cira.kyoto-u.ac.jp
http://dx.doi.org/10.1016/j.stemcr.2014.10.013
This is an open access article under the CC BY license (http://creativecommons.org/licenses/by/3.0/).

SUMMARY

Duchenne muscular dystrophy (DMD) is a severe muscle-degenerative disease caused by a mutation in the dystrophin gene. Genetic correction of patient-derived induced pluripotent stem cells (iPSCs) by TALENs or CRISPR-Cas9 holds promise for DMD gene therapy; however, the safety of such nuclease treatment must be determined. Using a unique k-mer database, we systematically identified a unique target region that reduces off-target sites. To restore the dystrophin protein, we performed three correction methods (exon skipping, frameshifting, and exon knockin) in DMD-patient-derived iPSCs, and found that exon knockin was the most effective approach. We further investigated the genomic integrity by karyotyping, copy number variation array, and exome sequencing to identify clones with a minimal mutation load. Finally, we differentiated the corrected iPSCs toward skeletal muscle cells and successfully detected the expression of full-length dystrophin protein. These results provide an important framework for developing iPSC-based gene therapy for genetic disorders using programmable nucleases.

INTRODUCTION

Duchenne muscular dystrophy (DMD) is a severe muscular degenerative disease caused by loss-of-function mutations in the dystrophin gene located on the X chromosome. The dystrophin gene consists of 79 exons, and disruption of the protein reading frame by small deletions, exon duplications, or loss of exons leads to DMD (Pichavant et al., 2011). The large size of the dystrophin gene hampers the delivery of therapeutic cDNA for gene augmentation. Therefore, the delivery of truncated microdystrophin or microutrophin by an adeno-associated viral (AAV) vector (Okada and Takeda, 2013), lentiviral vector (Pichavant et al., 2011), or *Sleeping Beauty* transposon (Filareto et al., 2013) has been investigated for DMD gene therapy. However, restoration of the full-length dystrophin protein remains challenging. An exon-skipping approach that modulates mRNA splicing patterns using antisense oligonucleotides (Aartsma-Rus et al., 2009) has shown promising results in preclinical studies, but the effects are only transient. Genomic correction using programmable nucleases is an ideal approach that can correct the mutated dystrophin gene.

The development of programmable nucleases has provided a powerful tool for modifying target genome sequences. In particular, the transcription activator-like effector nuclease (TALEN) (Hockemeyer et al., 2011) and the clustered regularly interspaced short palindromic repeat (CRISPR) and CRISPR associated 9 (Cas9) endonuclease systems (Cong et al., 2013; Mali et al., 2013) provide greater flexibility than meganucleases or zinc-finger nucleases (ZFNs) with regard to selecting the target regions of interest (Li et al., 2014). Several studies have demonstrated the effectiveness of TALENs (Hockemeyer et al., 2011; Ding et al., 2013a) and CRISPR (Ding et al., 2013b; Mali et al., 2013) in human induced pluripotent stem cells (iPSCs) for reporter knockin, gene knockout, and gene correction. In fact, corrections of disease mutation by nucleases in iPSCs have been reported for several diseases, including α1-antitrypsin deficiency (Choi et al., 2013), epidermolysis bullosa (Osborn et al., 2013), β-thalassemia (Ma et al., 2013), AIDS (Ye et al., 2014), and Niemann-Pick Type C (Maetzel et al., 2014).

Before the TALEN and CRISPR systems can reach clinical application, however, target specificity must be improved, as high off-target mutagenesis rates in human cells have been reported (Fu et al., 2013; Hsu et al., 2013; Lin et al., 2014), although some reports have shown otherwise (Smith et al., 2014; Suzuki et al., 2014; Veres et al., 2014). Since target specificity depends on the design of the target site, the properties of the DNA-binding domain, and the epigenetic status of the targeting site, the risk of off-target mutagenesis should be examined with respect to each targeting nuclease in a therapeutic setting.
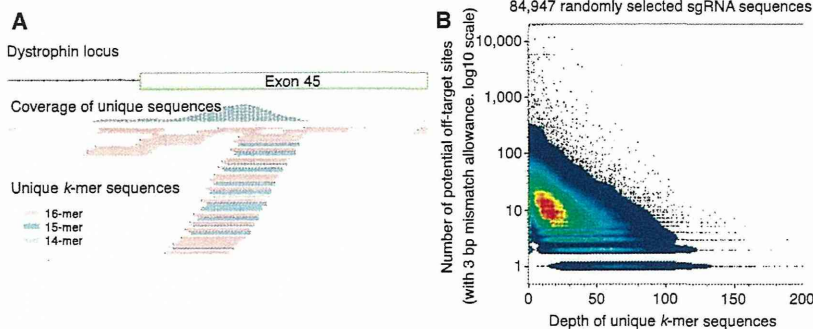
Figure 1. Visualization of the Unique Sequences in the Human Genome

(A) Example of the mapped unique k-mer sequences at the exon 45 region of the dystrophin gene. The mapped k-mers are indicated in the bottom panel and the coverage of the k-mers in each base position is indicated by the gray histogram. Within this region, unique sequences of 14- to 16-mer were identified.

(B) Pseudocolor dot plot for the depth of unique k-mers and the number of potential off-target sites. CRISPR-sgRNA targeting sequences (23 bp with "NGG" PAM, n = 84,947) were randomly selected from the human genome and the depth of the unique k-mers and number of potential off-target sites (with up to 3 bp mismatches allowance) for each sgRNA sequence were calculated. Note that higher depth correlated with fewer potential off-target sites. See also Table S1.

Immortalized myoblasts have been used for restoration of the dystrophin protein mediated by meganucleases (Rousseau et al., 2011; Popplewell et al., 2013), ZFNs (Rousseau et al., 2011), or TALENs (Ousterout et al., 2013). However, although primary myoblasts can be derived from patients, their clonal expansion requires transformation by oncogenes such as hTERT. In contrast, iPSCs (Takahashi et al., 2007) can be isolated from patients directly and still maintain pluripotency and an unlimited self-renewal capacity. Accordingly, when conjugated with made-to-order genetic correction technologies, human iPSCs derived from a patient with a genetic disorder (Park et al., 2008; Hotta et al., 2009) might be applicable to autologous transplantation as ex vivo gene therapy (Sebastiano et al., 2011; Soldner et al., 2011; Zou et al., 2011a, 2011b).

In this study, as a proof-of-concept of such gene therapy for DMD, we performed and demonstrated genetic correction of the dystrophin gene in patient-derived iPSCs by using three different methods: (1) disruption of the splicing acceptor to skip exon 45, (2) introduction of small indels to modulate the protein reading frame, and (3) knockin of the missing exon 44 to restore the full protein coding region. We then performed comprehensive genome-wide mutation analyses to assess the risk of off-target mutagenesis in 14 iPSC clones treated according to the TALEN or CRISPR approach. Our results demonstrate that genetic correction by these approaches in patient-derived iPSCs considerably lowers the risk of off-target mutagenesis and thus holds promise for DMD gene therapy.

RESULTS

Targeting a Unique Region in the Human Genome

The risk of off-target mutagenesis by programmable nucleases is associated with the specificity of the target sequence. For example, in the 23 bp of the single-guide RNA (sgRNA)

targeting region, up to 5 bp mismatches may be tolerated, which may lead to off-target mutagenesis (Fu et al., 2013; Hsu et al., 2013). To avoid this, the target sequence must be uniquely defined in the genome. Moreover, the uniqueness should be preserved when considering fragments of the sequence (i.e., 15 bp in length). Therefore, to systematically identify short unique sequences in the genome, we computationally generated all possible combinations of short k-mer sequences ($k \leq 16$) and searched the human genome to determine how many identical sequences are found for each k-mer sequence. We then extracted the unique k-mer sequences only when they matched a single location (i.e., with no match to other regions; see Table S1 available online). We stacked the mapped k-mer sequences as a histogram to visualize their uniqueness in the sequence depth of coverage (Koehler et al., 2011; Figure 1A). We confirmed that the higher the depth of the unique k-mer, the lower was the number of off-target sites, with up to 3 bp mismatches allowed (Figure 1B). Therefore, the genome regions with a higher depth of unique k-mers were considered good candidates for targeting by programmable nucleases, and regions with no peak were not considered. The benefit of this method is that it allows one to visually identify the targetable site quickly. Based on the histogram of the unique k-mers, we identified the 5' region of exon 45 in the dystrophin gene as a target site for designing TALENs and CRISPR-sgRNAs (Figures 2B and S2A).

Generation of Integration-free DMD iPSCs

A DMD patient was diagnosed with a deletion of dystrophin exon 44 by a multiplex ligation-dependent probe amplification method. We performed a primer walking method to sequence the deleted region and identified that the deleted size was 75,484 bp (chrX: 32,215,020-32,290,503 [hg19]), including exon 44 (Figure S1A). We generated iPSC lines from fibroblasts obtained from this DMD patient using
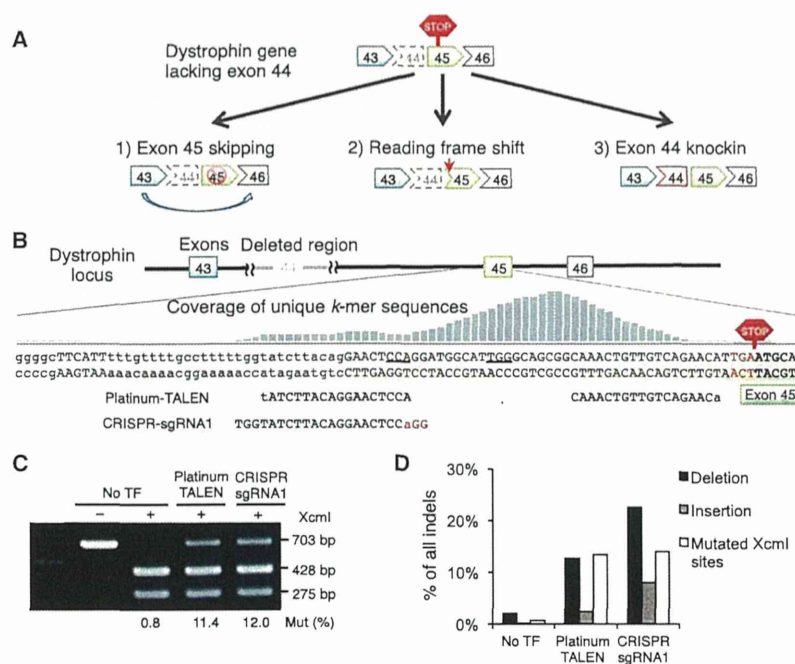
Figure 2. TALEN and CRISPR-sgRNA Are Equally Active for Targeting the Dystrophin Gene in iPSCs

(A) The three strategies used to restore the reading frame of the dystrophin protein.

(B) We designed the Platinum-TALEN pair and CRISPR-sgRNA1 within the peak of the unique *k*-mer sequences, as indicated by the gray histogram, and in front of the de novo premature stop codon, as indicated by the red hexagon.

(C) The activities of Platinum-TALEN and CRISPR-sgRNA1 were analyzed by a restriction enzyme (XcmI) sensitivity assay. The XcmI digestion site (CCANNNNNNNNNTGG) was located in the spacer of the TALEN and next to the PAM sequence of the CRISPR-sgRNA1. The intensity percentage of the undigested band (703 bp) was used to calculate the mutation efficiency.

(D) The frequency of deletions (black bar) and insertions (gray bar) was analyzed by deep sequencing for the region flanking the target site. The percentages of sequence reads corresponding to deletions, insertions, and mutated XcmI sites (white bar) are plotted. No TF, nontransfected control.

See also Figure S2.

the integration-free episomal vector method (Okita et al., 2011). We chose iPSC lines that maintained a normal karyotype (Figure S1B) and expressed pluripotency markers, including TRA-1-60, SSEA5, *OCT3/4*, and *NANOG* (Figures S1C and S1D). Pluripotency was also confirmed by the in vivo teratoma formation assay (Figure S1E).

Strategies for Dystrophin Correction

To restore the dystrophin protein reading frame in iPSCs from the DMD patient who lacked exon 44, we devised three approaches: the first was to disrupt the splicing acceptor of exon 45, as the connection of exons 43 and 46 would restore the reading frame; the second was to induce a frameshift by introducing small indels (insertions or deletions); and the third was to insert exon 44 in front of exon 45 (Figure 2A). We tested 15 pairs (five left and three right) of TALENs using the Golden-Gate assembly method (Golden-TALENs) (Sakuma et al., 2013a) and one pair of Platinum-Gate-based TALENs (Platinum-TALENs) (Sakuma et al., 2013b), which had nonrepeat-variable diresidue variations on the TAL domain to enhance the activity. We found that the E/a pair of Golden-TALENs and Platinum-TALENs showed the highest recombination activity, as assessed by the single-strand-annealing (SSA) assay, in human embryonic kidney 293T (HEK293T) cells (Figures S2B and S2C).

We also constructed five CRISPR-sgRNAs adjacent to the TALEN cleavage sites and tested the cleavage activities us-

ing the SSA assay (Figure S2C). There were no significant differences in the cleavage activities among the constructed CRISPR-sgRNAs. Therefore, we used sgRNA1 for later experiments because it was located within exon 45 and closer to the splicing acceptor than the other sequences. We then compared the activity of Platinum-TALEN and CRISPR-sgRNA1 by performing a restriction enzyme sensitivity assay, and found that both had similar activity in DMD iPSCs (Figure 2C).

When we examined the mutation patterns by deep amplicon sequencing of the target region, we found that both TALEN and CRISPR gave similar percentages of "mutated XcmI sites," which was consistent with the XcmI-digested sensitivity assay (Figures 2C and 2D). Interestingly, CRISPR induced a slightly higher indel rate compared with TALEN (Figure 2C), which suggested that the restriction enzyme sensitivity assay is sensitive to the relative position of the nuclease-targeting site and to restriction enzyme sites that differ by only a few basepairs. We also noted that TALEN produced fewer insertions compared with CRISPR-Cas9 (Figure 2D).

Correction of the Reading Frame Mutation Solely by Nuclease Treatment

We next utilized the programmable nucleases to restore the reading frame via disruption of the splicing acceptor (exon skipping) or induction of a ($3n + 1$) bp frameshift (where
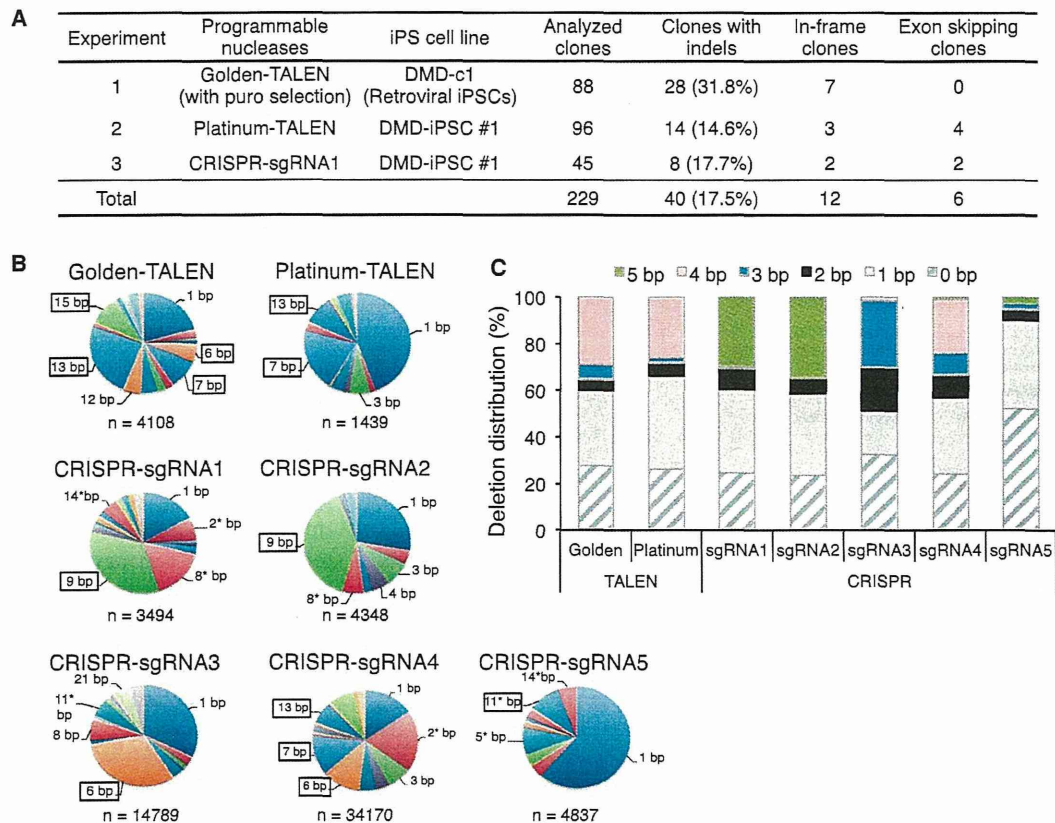
– 246 –

A

Experiment	Programmable nucleases	iPS cell line	Analyzed clones	Clones with indels	In-frame clones	Exon skipping clones
1	Golden-TALEN (with puro selection)	DMD-c1 (Retroviral iPSCs)	88	28 (31.8%)	7	0
2	Platinum-TALEN	DMD-iPSC #1	96	14 (14.6%)	3	4
3	CRISPR-sgRNA1	DMD-iPSC #1	45	8 (17.7%)	2	2
Total			229	40 (17.5%)	12	6

Figure 3. Correction of the Dystrophin Gene by Exon Skipping and Frameshifting Solely by Nuclease Treatment

(A) Summary of the exon-skipping (ES) and in-frame (IF) correction approaches using the indicated nucleases without the donor template. The DMD-c1 iPSC clone was derived by a retroviral method and the DMD-iPSC #1 (CiRA00111) clone was derived by an integration-free episomal vector method. Sanger sequence analyses were performed for all picked clones to identify subclones that had indels. The number of ES and IF clones is indicated.

(B) The deletion patterns induced by TALENs and CRISPR-sgRNAs were analyzed by deep sequencing of the target site. The numbers around the pie charts indicate the deletion sizes found in more than 5% of sequence reads, and the numbers with an asterisk indicate deletions that could restore the reading frame of the dystrophin gene. The boxed numbers indicate the deletion patterns flanked with local microhomologies.

(C) For each of the sequence reads obtained by deep sequencing, microhomology motifs on both sides of the deletion were retrieved and the distribution of the microhomology sizes was plotted.

See also Figure S3 and Table S2.

n is a nonnegative integer) without a donor template (frameshifting). Platinum-TALEN or CRISPR/Cas9-sgRNA1 was introduced into DMD iPSCs and the subclones were screened by Sanger sequencing of the target genomic DNA (Figures S3A and S3B). As summarized in Figure 3A, a total of 229 iPSC clones were analyzed, and 40 clones showed indels at the target site. Among the 40 clones with indels, six were identified as exon-skipping (ES) clones and 12 were identified as frameshift-induced in-frame (IF) clones. We chose two clones (ES[H19] and ES[H29]) with an 18 bp deletion spanning the splicing acceptor site of exon 45, and three clones (IF[H13], IF[H30], and IF[D28])

with a 1 bp insertion as IF clones with minimal alterations to the amino acid sequence (Figure S3B). We confirmed the pluripotency of the genetically corrected clones by examining their expression of OCT3/4, NANOG, TRA-1-60, and SSEA5 (Figures S1D and S3C). Functional pluripotency was also confirmed by a teratoma formation assay (Figure S3D).

Deletion Patterns Induced by TALENs and CRISPRs

In our indel pattern analysis, we observed that several clones harbored identical indel patterns mediated by flanking microhomology motifs. To further assess the indel
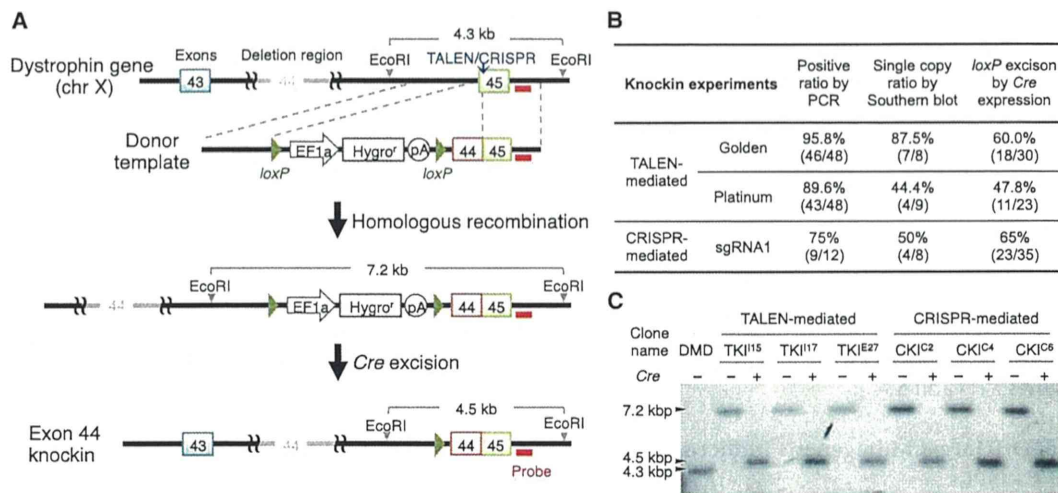
Figure 4. Correction of the Full-Length Dystrophin Protein by Exon 44 Knockin

(A) Schematic overview depicting the exon 44 knockin strategy. Top line: structure of the dystrophin gene with the exon 44 deletion. The vertical blue arrow indicates the TALEN/CRISPR cut site and the red bar indicates the intron 45 probe used for Southern blot analysis. Note that we introduced silent mutations at the nuclease-targeting site within exon 45 of the donor template.

(B) Summary of the exon 44 knockin experiments. The picked clones were first screened by genomic PCR for targeted knockin of the donor template and then by Southern blotting with EcoRI digestion and the intron 45 probe to confirm no additional integration. Successfully targeted clones were further treated with Cre to remove the drug selection cassette flanked by the loxP elements.

(C) Southern blot of the knockin clones (clone names: TKI^{I15}, TKI^{I17}, and TKI^{E27} for TALEN-mediated knockin clones; CKI^{C2}, CKI^{C4}, and CKI^{C6} for CRISPR-mediated knockin clones) showing successful targeting at the designated site. Subsequent Cre treatment excised the loxP-flanked drug selection cassette. The probe in intron 45 was used to detect EcoRI-digested genomic DNA fragments.

See also Figures S3B and S3C.

patterns, we isolated the genomic DNA 2–3 days after nuclease transfection (to avoid the effects of cellular expansion) and analyzed them by deep sequencing of amplicons. We observed several variations of indel patterns, but some sizes of deletions were enriched in both TALEN- and CRISPR-treated samples (Figure 3B). Computational analysis of the nuclease target site (In silico Genome Editing and Analysis Tools, https://apps.cira.kyoto-u.ac.jp/igeats/) led us to observe that microhomology motifs existed on both sides of the deletion site (Table S2), consistent with a recent report (Bae et al., 2014a). In our case, we found that the 3–5 bp microhomology-mediated deletions led to more than 30% of the deletion events analyzed (Figure 3C). This observation suggests that a cleavage site flanked by microhomology sequences can generate preferential deletion patterns, potentially via microhomology-mediated repair.

Correction of the Full-Length Dystrophin Protein with a Donor Template

The deletion of exon 44 is the third or fourth most common deletion in DMD patients (Aartsma-Rus et al., 2009; Tuffery-Giraud et al., 2009); however, the breakpoints of each deletion vary among patients. In order to restore the full amino acid sequence of the dystrophin protein for DMD patients who lack exon 44, we attempted to knock in the deleted exon 44 in front of exon 45. We constructed a donor template vector to conjugate exon 45 with exon 44 to share the same splicing acceptor site together with a hygromycin-selection cassette flanked by two loxP sites (Figure 4A). We utilized Golden-TALEN (E/a), Platinum-TALEN, and CRISPR-sgRNA1 for the knockin experiments.

The targeting donor was coelectroporated with TALENs or Cas9/sgRNA expression vectors. After hygromycin selection and limiting dilution, we isolated several clones and screened for knockin clones by PCR analysis. Regardless of which nuclease we used, up to 90% of the analyzed clones (46/48 for Golden-TALEN (E/a), 43/48 for Platinum-TALEN, and 9/12 for CRISPR-sgRNA1) showed targeting of the donor template at the target locus. We further confirmed single-copy knockin clones by Southern blot analysis and found that approximately 44%–87% of the clones had a single copy at the targeted site (Figure 4B). We chose two clones (TKI^{I15} and TKI^{I17}) mediated by Golden-TALEN (E/a), one clone (TKI^{E27}) mediated by Platinum-TALEN, and three clones (CKI^{C2}, CKI^{C4} and CKI^{C6}) mediated by CRISPR-sgRNA1 for the subsequent experiments.

To remove the selection cassette from the knockin clones, we transiently treated the obtained clones with the *Cre* expression vector to excise the hygromycin-selection cassette. Successful excision was confirmed by genomic PCR and Southern blotting (Figure 4C). We also sequenced the chimeric exon 44-45 in the knockin clones by Sanger sequencing, and detected no extra mutations except for the five silent mutations (underscored in Figure S3B) that were designed to prevent the sequence from being recut by our programmable nucleases. In addition, we checked the expression of the pluripotency markers *OCT3/4*, *NANOG*, TRA-1-60, and SSEA5 in the knockin clones (Figures S1D and S3C).

Analyses of Off-Target Mutagenesis Induced by TALENs or CRISPRs

The risk of undesired off-target mutagenesis is one of the most important concerns for the application of genome-editing technologies, and especially for gene therapy. We designed our experiments so that all genetically corrected clones originated from a single DMD-iPSC clone, which allowed us to distinguish preexisting genetic variations or culture artifacts in iPSCs (Laurent et al., 2011; Sugiura et al., 2014) from nuclease-mediated mutagenesis. The off-target effects were classified into two categories: target-sequence-dependent and -independent mutations. To assess the former, we searched for potential off-target sites with several mismatches in the human genome using the Bowtie program. For the Platinum-TALEN and Golden-TALEN E/a pair target sequences, we found thousands of potential off-target sites containing up to three mismatches for one side of TALEN. However, no pairs were located within 100 bp to form the FokI dimer. For the CRISPR-sgRNA1, we found five predicted off-target sites containing up to three mismatches (Figure S4A).

To investigate whether these potential off-target sites were actually mutated, we amplified the predicted off-target regions and analyzed them using the T7 endonuclease I (T7EI) assay. In contrast to the on-target cleavage, four predicted off-target sites showed no detectable mutagenesis, whereas one locus had a homozygous insertion of the AluYb9 element with a poly A tail (39-mer) (Figure S4B). The poly A stretch generated a heteroduplex when the PCR products were reannealed during the T7EI assay, resulting in digestion by T7EI even in the nontransfected control. We confirmed that the insertion of AluYb9 occurred in the original DMD fibroblasts and DMD iPSCs, but not in Caucasian-derived control iPSCs (Takahashi et al., 2007; Figure S4C).

To investigate the presence of minor mutations that were not detectable by the T7EI assay, we performed deep sequencing of the amplicons at the off-target sites. No significant indel reads were observed above the background level of the nontransfected control (Figure S4D).

Next, we examined whether nuclease treatment affected the chromosomal structure at the single-cell level. We first checked the karyotype of the genetically modified clones by performing a chromosome count with conventional Giemsa staining and high-resolution G-banding. Several suspected clones identified by G-banding were further analyzed by multicolor fluorescence in situ hybridization or multicolor banding. The majority of the modified cells (144/153, 94.1%) maintained a normal karyotype (Figures 5A and S5), but a few (9/153, 5.9%) showed a suspected or abnormal karyotype in three clones (out of seven modified clones analyzed; Figures S5D and S5E). Interestingly, it was previously reported that an amplification of chr20q11.21 was associated with a growth advantage for human embryonic stem cells (Amps et al., 2011). With the TKI[117] clone, we observed an inverted insertion at chr20q11.2 (ins(20)p11.2q13.3q12) in two of the 30 metaphases we analyzed. This insertion may have been acquired during the subcloning process.

It was previously reported that TALENs or CRISPR-Cas9 may induce up to 1 Mbp of deletions if two separated sites are targeted simultaneously (Canver et al., 2014). To elucidate whether the off-target cleavage of TALENs or CRISPR-Cas9 induced such large deletions or duplications, we investigated DNA copy number variations (CNVs) in the corrected clones by TALEN or CRISPR treatment with a high-density SNP array. We detected several CNVs compared with the reference data (human population mean), including the 75 kbp deletion of dystrophin exon 44, validating our analysis (Figure S6).

We focused on the de novo CNVs that were not present in the original DMD iPSCs, and found no major differences in the number of CNVs among the three corrected groups (Figure S6B). We employed three control clones that were subjected to similar electroporation and limiting dilution processes as the dystrophin-corrected clones, but were unmodified at the target site. To determine whether there was any correlation between the potential off-target sites and the observed CNVs, we measured the distance between the edges of the CNVs and the potential nuclease cleavage sites. The distributions for each nuclease were comparable to the corresponding numbers of randomly selected genomic loci (Figure 5B).

Furthermore, we sequenced the whole protein-coding regions of the original DMD-iPSC clone and their subclones by exome sequencing (Table S3). To assess the single nucleotide mutations associated with the treatment of programmable nucleases, we used the parental DMD iPSC as a reference and extracted the de novo mutations observed only in the offspring clones. From this analysis,

A Karyotype analyses for DMD-iPSC and the corrected clones

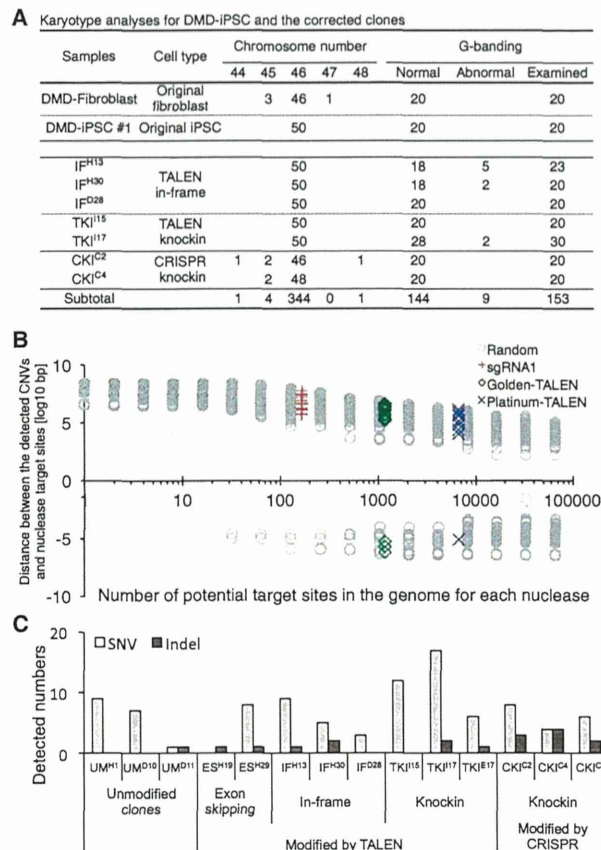| Samples	Cell type	Chromosome number					G-banding		
		44	45	46	47	48	Normal	Abnormal	Examined
DMD-Fibroblast	Original fibroblast		3	46	1		20		20
DMD-iPSC #1	Original iPSC			50			20		20
IF^{H13}	TALEN in-frame			50			18	5	23
IF^{H30}				50			18	2	20
IF^{D28}				50			20		20
TKI^{I15}	TALEN knockin			50			20		20
TKI^{I17}				50			28	2	30
CKI^{C2}	CRISPR knockin	1	2	46		1	20		20
CKI^{C4}			2	48			20		20
Subtotal		1	4	344	0	1	144	9	153

B

C

Figure 5. Multiple Whole-Genome Analyses Revealed No Severe Off-Target Mutagenesis

(A) Summary of the karyotyping analyses of the corrected clones. Conventional Giemsa staining was used for chromosome counting (50 metaphases were counted), and high-resolution G-banding was applied to detect chromosomal rearrangements (at least 20 metaphases were analyzed).

(B) SNP array analysis identified de novo CNVs in the corrected clones. To determine associations between detected CNVs and potential off-target sites, the distances between the edges of the detected CNVs and potential nuclease target sites are plotted for each nuclease (red cross for sgRNA1, green diamond for Golden-TALEN, and blue × mark for Platinum-TALEN). Since the likelihood of the distance distribution depends on how many genomic sites are selected, we also selected random genomic positions and calculated the distance for each CNV (gray circles). A zero value in the y axis indicates the edge of the CNVs and a negative value indicates the inside of the CNVs. If any given nuclease off-target site is associated with the detected CNVs, the target site should approximate zero distance.

(C) The number of single nucleotide variants (SNVs) and small indels detected by exome sequencing. Only de novo SNVs and indels that did not exist in the original DMD fibroblasts or DMD iPSCs are plotted. Unmodified control clones underwent the same electroporation and subcloning process as the other corrected clones and were sequenced at similar passage numbers.

See also Figures S4–S6 and Tables S3–S5.

we identified a few dozen point mutations (both synonymous and nonsynonymous) and several indels from the exome sequencing data (Figure 5C; Tables S4 and S5). Importantly, we successfully detected the 1 bp insertion and 18 bp deletion at the dystrophin exon 45 in the IF and ES clones, respectively (Table S5, labeled in blue). We observed slightly higher indel events ($p < 0.05$, one-way ANOVA) in the CRISPR knockin clones (average 3.0) compared with the unmodified controls (average 0.33). However, most of the detected indels were in the triple-repeat or GC-rich regions and were not associated with potential off-target sites, which is consistent with recent reports (Smith et al., 2014; Veres et al., 2014). In addition, there were no significant differences in the number of SNVs among the three correction approaches and the control group ($p > 0.05$, one-way ANOVA), which is also in agreement with recent publications (Smith et al., 2014; Veres et al., 2014). Taken together, these results show that no severe off-target mutagenesis was associated with potential nuclease-targeting sites in the dystrophin-corrected iPSC clones.

The Dystrophin Protein Was Restored in Differentiated Skeletal Muscle Cells

To confirm that genetic correction by TALEN and CRISPR resulted in restoration of the dystrophin gene products, we differentiated the original and corrected iPSC clones into skeletal muscle cells using our recently published method (Tanaka et al., 2013). Differentiated skeletal muscle cells were collected on day 9 of differentiation to isolate mRNA. Amplification using PCR primers spanning exons 43 and 46 revealed that the exon 44 knockin clone (CKI^{C2}) had restored the full-length dystrophin mRNA to the same length as that of a healthy individual control ("Healthy"; Figure 6A). Sanger sequence analysis of the cDNA also showed the corresponding correction, where the 1 bp insertion of "A" in the IF clone (IF^{H30}), the 18 bp deletion that induced the skipping of exon 45 (ES^{H29}), and the knockin clone (TKI^{I15} and CKI^{C2}) all led to successful expression of the inserted exon 44 together with exon 45 (Figure 6B).

Finally, to detect the restored dystrophin protein, we performed immunofluorescence staining with an anti-dystrophin antibody (Dys1), which recognizes the rod domain (amino acids 1,181–1,388) of the dystrophin protein (Figure 6C). The restored dystrophin protein was localized at the submembrane region, as expected, in all corrected clones examined. Furthermore, we performed a western blot analysis with an anti-dystrophin antibody, which recognizes amino acids 3,661–3,677, and detected bands at the following predicted sizes: 420 kDa for the reading-frame corrected clone, 414 kDa for the ES clone, and 427 kDa for the knockin clone (Figure 6D). As expected,